

Single-Scanline Relative Pose Estimation for Rolling Shutter Cameras

Petr Hruby
ETH Zürich
Rämistrasse 101, 8006 Zürich
petr.hruby@inf.ethz.ch

Marc Pollefeys
ETH Zürich / Microsoft Spatial AI Lab
Rämistrasse 101, 8006 Zürich
marc.pollefeys@inf.ethz.ch

Abstract

We propose a novel approach for estimating the relative pose between rolling shutter cameras using the intersections of line projections with a single scanline per image. This allows pose estimation without explicitly modeling camera motion. Alternatively, scanlines can be selected within a single image, enabling single-view relative pose estimation for scanlines of rolling shutter cameras. Our approach is designed as a foundational building block for rolling shutter structure-from-motion (SfM), where no motion model is required, and each scanline’s pose can be computed independently. We classify minimal solvers for this problem in both generic and specialized settings, including cases with parallel lines and known gravity direction, assuming known intrinsics and no lens distortion. Furthermore, we develop minimal solvers for the parallel-lines scenario, both with and without gravity priors, by leveraging connections between this problem and the estimation of 2D structure from 1D cameras. Experiments on rolling shutter images from the Fastec dataset demonstrate the feasibility of our approach for initializing rolling shutter SfM, highlighting its potential for further development. The code will be made publicly available.

1. Introduction

Relative pose estimation is a fundamental problem in computer vision with applications in Structure from Motion [62], SLAM, multi-view stereo, and visual odometry. This paper focuses on estimating relative pose between rolling shutter (RS) cameras.

Rolling shutter cameras capture images row by row. If the camera is static during capture, the resulting image is equivalent to that of a pinhole camera. However, if the camera moves, the rolling shutter effect distorts the image, making standard pinhole-based methods [49] unreliable.

A common approach to handle rolling shutter distortion is modeling camera motion with parametric models such as SLERP [65], Cayley transformation [26], linearized

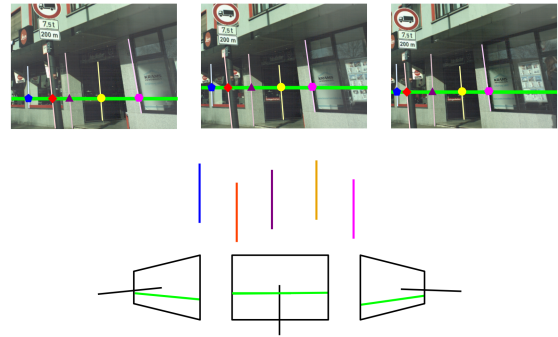


Figure 1. We estimate a relative pose from the intersections of the line projections with a single scanline per image (green). This allows us to estimate relative pose between rolling shutter cameras without modelling the camera motion.

rotation [4], affine motion [69], pushbroom [47], accelerated motion [19], or order-one motion [24]. This has been successfully applied to absolute pose estimation [2–6, 9, 33, 34, 37, 45, 46, 60], bundle adjustment [28, 42, 43, 48, 61, 63, 73, 76], SfM [27, 32, 59], and motion rectification from single cameras [36, 52, 53, 57, 74, 79], camera rigs [1, 7, 20, 64], and videos [14, 19, 21, 23, 31, 54, 55, 58, 69, 70, 77].

While most methods use point-based features, some employ lines for absolute pose estimation [3], bundle adjustment [76], and motion rectification [36, 52, 53, 57].

The problem of estimating relative pose for rolling shutter cameras has been explored in prior work. Special essential matrices for RS cameras under different motion models were introduced in [15], along with linear non-minimal solvers. The problem was also solved for pure translation models with constant velocity and acceleration [78]. IMU-based approaches reduced the required number of point correspondences from 11 to 5 [39, 40]. Other methods first estimate pose using a global shutter solver before refining with an RS model [38]. Additional works estimate relative pose for RS camera rigs [72] and for planar scenes [35]. Recently, [24] classified RS relative pose minimal problems

under the order-one motion model. Despite this, the general RS relative pose problem remains unsolved.

One drawback of parametric motion models is their reliance on an assumed motion that may not match real-world trajectories. An alternative is estimating pose independently for each scanline, similar to line-camera calibration [29, 41, 67, 71, 75]. This approach has been used for tracking a single camera [10, 11] and a camera rig [16] with respect to a predefined marker.

We explore the feasibility of estimating relative pose between scanlines of RS cameras, without explicit motion modelling. The goal is to use this method as a building block to initialize rolling-shutter SfM where no motion model is required and each scanline can have its pose independently computed. To the best of our knowledge, this is the first work that enables this. After the initialization, scanlines from remaining images may be registered by solving the generalized relative pose problem [66], similarly to [10, 11, 16], or, in the case of a planar scene, using [9]. Our contributions include:

- Formulation of the problem of relative pose estimation from line projections in a single scanline per image, assuming known intrinsics and no lens distortion.
- Enumeration of minimal problems for general and specialized settings with parallel lines and gravity priors.
- Demonstration that the problems with parallel lines and with vertical lines and gravity prior correspond to estimating relative pose of uncalibrated cameras [56], respectively calibrated [8] 1D camera pose.
- Development of minimal solvers for the following cases:
 - 3 cameras, 7 parallel lines (with projective ambiguity).
 - 3 cameras, gravity prior, 7 parallel lines.
 - 3 cameras, gravity prior, 5 vertical lines.
 - 4 cameras, gravity prior, 4 vertical lines.
- Evaluation of solvers on synthetic and real RS datasets (Fastec, [44]), taking scanlines either from *different images* or from a *single image*.

1.1. Notation

We use bold letters for matrices and vectors, and normal font for scalars. Indexing starts from one, with indices in brackets; e.g., the first element of \mathbf{L}_d is $\mathbf{L}_{d(1)}$. Matrix indexing follows Matlab style, where $\mathbf{A}_{(:,1:2)}$ selects the first two rows of \mathbf{A} . The scanlines are denoted with a scalar $y \in \mathbb{R}$ giving their y-coordinate. The set of all 3D lines is denoted as $Gr(1, 3)$.

2. Problem Formulation

This section describes the geometry of a line projected into a rolling-shutter camera and derives an algebraic constraint useful for estimating camera poses.

Consider n rolling-shutter cameras capturing the same 3D scene. Due to motion, the cameras capture different

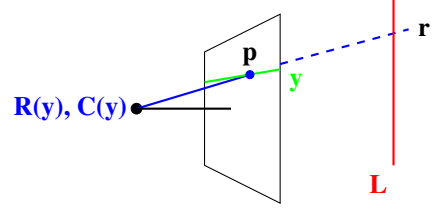


Figure 2. Illustration of the line projection. Line \mathbf{L} projects onto scanline y at point \mathbf{p} . Then, the ray \mathbf{r} obtained by backprojecting \mathbf{p} intersects \mathbf{L} , yielding the constraint (3).

rows at different poses. Let $\mathbf{R}_i(y) \in SO(3)$ and $\mathbf{C}_i(y) \in \mathbb{R}^3$ denote the orientation and center of camera i at row y .

We aim to estimate the relative pose between the cameras without explicitly modeling their motion functions. To achieve this, we select a single row y_i per camera and measure intersections between these selected rows and the projections of m straight lines $\mathbf{L}_j \in Gr(1, 3)$. Then, we use this information to recover the camera poses $\mathbf{R}_i(y_i)$, $\mathbf{C}_i(y_i)$. Figure 1 illustrates the setup.

Let $\mathbf{p}_{i,j} \in \mathbb{P}^2$, with $p_{i,j} = [x_{i,j} \ y_i \ 1]^T$, denote the projection of line \mathbf{L}_j onto row y_i of camera i . Then, the backprojected ray $\mathbf{r}_{i,j}$ from $\mathbf{p}_{i,j}$ intersects line \mathbf{L}_j , giving:

$$\mathbf{r}_{i,j} = \mathbf{C}_i(y_i) + \lambda_{i,j} \mathbf{R}_i(y_i)^T \mathbf{p}_{i,j}, \quad \lambda_{i,j} \in \mathbb{R}. \quad (1)$$

This situation is depicted in Fig. 2. Let us represent \mathbf{L}_j with a pair $(\mathbf{L}_{0,j}, \mathbf{L}_{d,j})$, where $\mathbf{L}_{0,j}$ is a point on the line and $\mathbf{L}_{d,j}$ is its direction. The ray $\mathbf{r}_{i,j}$ intersects \mathbf{L}_j if and only if:

$$\exists \alpha, \beta \in \mathbb{R} : \quad \mathbf{C}_i(y_i) + \alpha \mathbf{R}_i(y_i)^T \mathbf{p}_{i,j} = \mathbf{L}_{0,j} + \beta \mathbf{L}_{d,j}. \quad (2)$$

This is equivalent to requiring that vectors $\mathbf{R}_i(y_i)^T \mathbf{p}_{i,j}$, $\mathbf{L}_{d,j}$, and $\mathbf{L}_{0,j} - \mathbf{C}_i(y_i)$ are linearly dependent. Since three 3D vectors are linearly dependent if and only if their scalar triple product vanishes, we obtain:

$$\mathbf{p}_{i,j}^T \mathbf{R}_i(y_i) [\mathbf{L}_{d,j}]_{\times} (\mathbf{L}_{0,j} - \mathbf{C}_i(y_i)) = 0. \quad (3)$$

Each projection provides a single constraint on the unknowns (lines and camera poses). A 3D line has four degrees of freedom, requiring four scanlines for triangulation and at least five scanlines for constraining relative pose.

2.1. Assuming parallel lines

Let us consider the scenario where all lines are parallel, which frequently occurs in real-world settings. Here, all lines share a common direction $\mathbf{L}_d \in \mathbb{R}^3$. Since Eq. (3) is invariant to scene rotation, we align \mathbf{L}_d with the y-axis, \mathbf{e}_2 . This allows representing each line \mathbf{L}_j with a single point $\mathbf{L}_{0,j}$ in the xz-plane, with its y-coordinate equal to zero.

With a shared direction, each line has only two individual degrees of freedom (DoF). Once \mathbf{L}_d is known, a line can be triangulated from just two cameras. This reduces the

minimum number of cameras needed for pose estimation to three. To simplify Eq. (3), we substitute \mathbf{e}_2 for $\mathbf{L}_{d,j}$:

$$\mathbf{p}_{i,j}^T \mathbf{R}_i(y_i) \left(\begin{bmatrix} \mathbf{L}_{0,j(3)} \\ 0 \\ -\mathbf{L}_{0,j(1)} \end{bmatrix} - \begin{bmatrix} \mathbf{C}_i(y_i)_{(3)} \\ 0 \\ -\mathbf{C}_i(y_i)_{(1)} \end{bmatrix} \right) = 0. \quad (4)$$

We define rotation $\mathbf{R}_{0,i} \in SO(3)$ around the x-axis, which maps row y_i to $y = 0$, and set $\mathbf{p}'_{i,j} = \mathbf{R}_{0,i} \mathbf{p}_{i,j}$. Then, there holds $\mathbf{p}'_{i,j} = [x'_{i,j} \ 0 \ 1]^T$. Defining

$$\begin{aligned} \mathbf{R}'_i &= \mathbf{R}_{0,i} \mathbf{R}_i(y_i), \\ \mathbf{t}'_i &= -\mathbf{R}_{0,i} \mathbf{R}_i(y_i) [\mathbf{C}_i(y_i)_{(3)} \ 0 \ -\mathbf{C}_i(y_i)_{(1)}]^T, \end{aligned} \quad (5)$$

and substituting \mathbf{R}'_i , \mathbf{t}'_i , and $\mathbf{p}'_{i,j}$ into Eq. (4), we obtain:

$$[x'_{i,j} \ 1]^T \begin{bmatrix} -\mathbf{R}'_{i(1,3)} & \mathbf{R}'_{i(1,1)} & \mathbf{t}'_{i(0)} \\ -\mathbf{R}'_{i(3,3)} & \mathbf{R}'_{i(3,1)} & \mathbf{t}'_{i(2)} \end{bmatrix} \begin{bmatrix} \mathbf{L}_{0,j(1)} \\ \mathbf{L}_{0,j(3)} \\ 1 \end{bmatrix} = 0. \quad (6)$$

We can write Equation (6) in a vector form as

$$\mathbf{u}_{i,j}^T \mathbf{A}_i \mathbf{L}_{h,j} = 0, \quad (7)$$

where $\mathbf{A}_i \in \mathbb{R}^{2,3}$ is a matrix encoding the camera pose, $\mathbf{u}_{i,j} \in \mathbb{P}^1$ is a vector encoding the observation, and $\mathbf{L}_{h,j} \in \mathbb{P}^2$ is a homogeneous representation of point $\mathbf{L}_{0,j}$. Alternatively, we define $\mathbf{u}'_{i,j} = [1 \ -x'_{i,j}]^T$, and rewrite (7) as

$$\lambda_{i,j} \mathbf{u}'_{i,j} = \mathbf{A}_i \mathbf{L}_{j,h}, \quad \lambda_{i,j} \in \mathbb{R}. \quad (8)$$

Since constraint (7) is homogeneous, matrix \mathbf{A}_i has 5 DoF. The elements $\mathbf{R}_i(y_i)$, $\mathbf{C}_i(y_i)_{(1)}$, $\mathbf{C}_i(y_i)_{(3)}$ of the pose, which appear in \mathbf{A}_i , also have 5 DoF. Using the Gröbner basis method, we have verified that for every matrix $\mathbf{A} \in \mathbb{R}^{2,3}$, there are 8 ways to decompose it into pose parameters $R \in SO(3)$, $C_{(1)} \in \mathbb{R}$, $C_{(3)} \in \mathbb{R}$, and a scale factor $\sigma \in \mathbb{R}$. This means that \mathbf{A}_i has no internal constraints, and every 2×3 matrix can represent \mathbf{A}_i for some pose.

Therefore, the relative pose problem can be transformed into finding matrices $\mathbf{A}_i \in \mathbb{R}^{2,3}$, vectors $\mathbf{L}_{h,j} \in \mathbb{P}^2$, and scalars $\lambda_{i,j} \in \mathbb{R}$ such that (8) holds for every $i \in \{1, \dots, n\}$, $j \in \{1, \dots, m\}$. This is equivalent to the problem of estimating 2D structure from images taken by n uncalibrated 1D cameras, which has been studied in [56].

2.1.1. Ambiguities in the case with parallel lines

The assumption that all lines are parallel introduces ambiguities into the relative pose estimation. First, since all line directions $\mathbf{L}_{d,j}$ are equal, the values of constraints (3) remain unchanged if we shift $\mathbf{C}_i(y_i)$ to $\mathbf{C}_i(y_i) + \gamma \mathbf{L}_{j,d}$ for any $\gamma \in \mathbb{R}$. Therefore, it is only possible to estimate the camera centers up to translation along \mathbf{L}_d .

Furthermore, if (8) holds for some $\mathbf{A}_i \in \mathbb{R}^{2,3}$, $\mathbf{L}_{h,j} \in \mathbb{P}^2$, then (8) also holds for $\mathbf{A}_i \cdot \mathbf{H}^{-1}$, $\mathbf{H} \cdot \mathbf{L}_{j,h}$ for every invertible $\mathbf{H} \in \mathbb{R}^{3,3}$. Therefore, the cameras and the structure can only be estimated up to a projective transformation \mathbf{H} .

We show later in the paper that we can resolve the projective ambiguity by introducing priors on the cameras. To resolve the ambiguity in the camera centers, we can, for instance, observe one line orthogonal to \mathbf{L}_d and use it to estimate the camera centers.

3. Enumerating minimal problems

In this section, we classify minimal problems for estimating the relative pose from projections of n lines onto m scanlines, along with their degrees. We consider five settings:

- A. **Fully generic setting**
- B. **Parallel lines**
- C. **Gravity prior for cameras + Generic lines**
- D. **Gravity prior for cameras + Parallel lines**
- E. **Gravity prior for cameras + Vertical lines**

In cases A and C, we estimate the pose up to global rotation, translation, and scale. In cases D and E, we estimate the pose up to these transformations and an additional shift of centers $\mathbf{C}_i(y_i)$ along direction \mathbf{L}_d . In case B, we estimate the pose up to these transformations, the shift of centers along \mathbf{L}_d , and the projective transformation \mathbf{H} .

For each setting, we determine the number of cameras m and the number of lines n s.t. the problem (3) is minimal. We assume *complete visibility*, meaning each line is projected into each camera. We follow concepts from [17]: *Minimal problem* [17, Def. 1]: A parametric polynomial system $f(\theta, \mathbf{x}) = 0$ with a finite nonzero number of solutions \mathbf{x}^* for a generic set of parameters θ .

Balanced problem [17, Def. 2]: A parametric polynomial system $f(\theta, \mathbf{x}) = 0$ where the dimensionality of the space of variables \mathbf{x} equals the number of independent equations. *Condition for minimal problems* [17, Step. 1, Corr. 2]: A problem $f(\theta, \mathbf{x}) = 0$ is minimal if and only if it is *balanced* and its Jacobian $\frac{\partial f(\theta, \mathbf{x}^*)}{\partial \mathbf{x}}$ is invertible for generic θ, \mathbf{x}^* .

This summary provides the foundation for enumerating minimal problems. For detailed theory, refer to [17]. In our case, the parameter vector θ consists of projections $\mathbf{p}_{i,j} \in \mathbb{P}^2$, and the variable vector \mathbf{x} encodes camera poses $(\mathbf{R}_i(y_i), \mathbf{C}_i(y_i))$ and lines $(\mathbf{L}_{0,j}, \mathbf{L}_{d,j})$. The polynomial system $f(\mathbf{x}, \theta)$ consists of equations in the form of (3). Following [17], we used the following steps to list all minimal problems and determine their degrees:

- Enumerate all balanced problems for each setting A–E.
- For each balanced problem, generate random camera poses and lines \mathbf{x}^* , reproject the lines into the cameras, and obtain projections θ such that $f(\theta, \mathbf{x}^*) = 0$.
- Compute the Jacobian $\frac{\partial f(\theta, \mathbf{x}^*)}{\partial \mathbf{x}}$. Label the problem as minimal if $\det \frac{\partial f(\theta, \mathbf{x}^*)}{\partial \mathbf{x}} \neq 0$.
- Use monodromy computation from [13] to determine the degree of minimal problems.

According to algebraic geometry, finding a single instance where the Jacobian is full-rank suffices to claim generic

S.	m	n	Min.	Deg	S.	m	n	Min.	Deg
A	5	23	Y	389k+	D	3	7	Y	48
A	21	7	Y	40k+	D	4	5	Y	232
B	3	7	Y	2*	D	6	4	Y	1224
B	4	6	Y	2*	E	3	5	Y	16
C	5	15	Y	1.8M+	E	4	4	Y	32
C	15	5	Y	532k+					

Table 1. List of balanced problems for settings A–E. S . denotes the setting, m and n are the number of cameras and lines, and Deg is the degree. Column Min. contains Y if the problem is minimal. 2* indicates two solutions in terms of 2×3 matrices, and + denotes computations that did not terminate. See Sec. 3 for details.

minimality. In the following subsections, we enumerate minimal problems for each setting A–E.

A. Fully Generic Setting Each camera has 6 degrees of freedom (DoF), while each line has 4 DoF. Due to gauge freedom, we fix 7 DoF (3 for rotation, 3 for translation, and 1 for scale). There are $m \cdot n$ constraints in the form of (3), fixing $m \cdot n$ DoF. The balanced constraint is therefore:

$$6m + 4n - 7 = mn. \quad (9)$$

We define a function $n_A(m)$, mapping the number of cameras m to the number of lines n , s.t. (9) holds for $m, n_A(m)$:

$$n_A(m) = \frac{6m - 7}{m - 4}. \quad (10)$$

As stated in Sec. 2, the minimal number of cameras is $m \geq 5$. The function $n_A(m)$ is strictly decreasing for $m > 4$, and since $\lim_{m \rightarrow \infty} n_A(m) = 6$, no balanced problem has fewer than 7 lines. Evaluating $n_A(m)$ for integer values of m from 5 onward, and searching for integer values of $n_A(m)$, we identify the following balanced cases:

- $m = 5, n = 23$; $m = 21, n = 7$

B. Parallel Lines As discussed in Sec. 2, the pose is estimated up to a shift along \mathbf{L}_d and a projective transformation $\mathbf{H} \in \mathbb{R}^{3 \times 3}$. The pose estimation corresponds to estimating matrices $\mathbf{A}_i \in \mathbb{R}^{2 \times 3}$ and points $\mathbf{L}_{h,j} \in \mathbb{P}^2$ such that (7) holds for all i, j . Here, each camera has 5 DoF, each line has 2 DoF, and we fix 8 DoF due to projective ambiguity. The balanced constraint is:

$$5m + 2n - 8 = mn. \quad (11)$$

Defining $n_B(m)$ as:

$$n_B(m) = \frac{5m - 8}{m - 2}, \quad (12)$$

and noting that $m \geq 3$, we find $\lim_{m \rightarrow \infty} n_B(m) = 5$, implying no balanced problem has fewer than 6 lines. Evaluating $n_B(m)$ for integer m , we obtain:

- $m = 3, n = 7$; $m = 4, n = 6$

C. Gravity Prior for Cameras + Generic Lines With a known vertical direction, each camera has 4 DoF (1 for rotation, 3 for translation), and we fix 5 DoF due to gauge freedom. Lines remain generic, contributing 4 DoF each. The balanced constraint is:

$$4m + 4n - 5 = mn. \quad (13)$$

The corresponding function is:

$$n_C(m) = \frac{4m - 5}{m - 4}. \quad (14)$$

We find $\lim_{m \rightarrow \infty} n_C(m) = 4$, so no balanced problem has fewer than 5 lines. Checking integer values of m , we get:

- $m = 5, n = 15$; $m = 15, n = 5$

D. Gravity Prior for Cameras + Parallel Lines Here, camera rotation has 1 DoF, and the camera center has 2 DoF (up to translation along the line). We fix 4 DoF due to gauge freedom. Lines share 2 DoF for direction \mathbf{L}_d , with each line having 2 additional DoF. The balanced constraint is:

$$3m + 2 + 2n - 4 = mn. \quad (15)$$

We get $n_D(m)$ as:

$$n_D(m) = \frac{3m - 2}{m - 2}. \quad (16)$$

For $m \geq 3$, we find $\lim_{m \rightarrow \infty} n_D(m) = 3$, meaning no balanced problem has fewer than 4 lines. We have found:

- $m = 3, n = 7$; $m = 4, n = 5$; $m = 6, n = 4$

E. Gravity Prior for Cameras + Vertical Lines Similar to the previous case, each camera has 3 DoF, and we fix 4 DoF due to gauge freedom. Since the direction \mathbf{L}_d is fixed, each line has 2 DoF. The balanced constraint is:

$$3m + 2n - 4 = mn. \quad (17)$$

We define $n_E(m)$ as:

$$n_E(m) = \frac{3m - 4}{m - 2}. \quad (18)$$

For $m \geq 3$, we find $\lim_{m \rightarrow \infty} n_E(m) = 3$, meaning no balanced problem has fewer than 4 lines. We found problems:

- $m = 3, n = 5$; $m = 4, n = 4$

All balanced problems for these settings are summarized in Table 1, along with their minimality status and degree. The table shows that problems with parallel/vertical lines (B, D, E) are minimal and computationally feasible. Problems with generic lines (A, C) are minimal but have degrees too high for practical RANSAC solutions. For problems (A, 5, 23) and (C, 5, 15), monodromy computations did not terminate within a month.

4. Minimal solvers

In this section, we introduce solvers for the minimal problems $(B, 3, 7)$, $(D, 3, 7)$, $(E, 3, 5)$, $(E, 4, 4)$ from Section 3. We use the notation and concepts from Sec. 2.

4.1. Parallel lines with generic cameras

Here, we describe the solution to the problem $(B, 3, 7)$. Since the lines are parallel, our goal is to find matrices $\mathbf{A}_1, \mathbf{A}_2, \mathbf{A}_3 \in \mathbb{R}^{2 \times 3}$ and vectors $\mathbf{L}_{h,j}$ for $j \in \{1, \dots, 7\}$, such that equation (7) holds for every camera i and line j . Due to projective ambiguity, we aim to recover the camera poses up to a common projective transformation $\mathbf{H} \in \mathbb{R}^{3 \times 3}$. Each camera triplet $\mathbf{A}_1, \mathbf{A}_2, \mathbf{A}_3$ can be expressed as:

$$\mathbf{A}_1 = \mathbf{A}_{c,1} \cdot \mathbf{H}, \quad \mathbf{A}_2 = \mathbf{A}_{c,2} \cdot \mathbf{H}, \quad \mathbf{A}_3 = \mathbf{A}_{c,3} \cdot \mathbf{H}, \quad (19)$$

for some $\mathbf{H} \in \mathbb{R}^{3 \times 3}$, with $\mathbf{A}_{c,1}, \mathbf{A}_{c,2}, \mathbf{A}_{c,3}$ taking the form:

$$\mathbf{A}_{c,1} = \begin{bmatrix} 1 & 0 & 0 \\ \alpha_1 & \alpha_1 & \alpha_1 \end{bmatrix}, \quad \mathbf{A}_{c,2} = \begin{bmatrix} 1 & 0 & 0 \\ \alpha_2 & \alpha_3 & \alpha_4 \end{bmatrix}, \quad \mathbf{A}_{c,3} = \begin{bmatrix} 1 & 0 & 0 \\ \alpha_5 & \alpha_6 & \alpha_7 \end{bmatrix}. \quad (20)$$

The proof follows analogously to Proposition 2 in [30]. These canonical-form matrices have 7 DoF.

To estimate $\mathbf{A}_{c,1}, \mathbf{A}_{c,2}, \mathbf{A}_{c,3}$, we leverage the fact that, as shown in [56], a trifocal tensor exists between three camera matrices $\mathbf{A}_i \in \mathbb{R}^{2 \times 3}$. To compute this tensor, we stack the constraints from (8) into the matrix equation:

$$\begin{bmatrix} \mathbf{A}_1 & \mathbf{u}'_{1,j} & 0 & 0 \\ \mathbf{A}_2 & 0 & \mathbf{u}'_{2,j} & 0 \\ \mathbf{A}_3 & 0 & 0 & \mathbf{u}'_{3,j} \end{bmatrix} \begin{bmatrix} \mathbf{L}_{h,j} \\ -\lambda_{1,j} \\ -\lambda_{2,j} \\ -\lambda_{3,j} \end{bmatrix} = 0. \quad (21)$$

For this equation to hold, the determinant of the coefficient matrix must vanish, leading to the constraint:

$$\sum_{a=1}^2 \sum_{b=1}^2 \sum_{c=1}^2 \mathbf{u}'_{1,j(a)} \mathbf{u}'_{2,j(b)} \mathbf{u}'_{3,j(c)} \mathbf{T}_{(a,b,c)} = 0, \quad (22)$$

where $\mathbf{T} \in \mathbb{R}^{2 \times 2 \times 2}$ is the trifocal tensor with elements:

$$\mathbf{T}_{(a,b,c)} = (-1)^{a+b+c} \det \left(\begin{bmatrix} \mathbf{A}_{1(a,:)}^T & \mathbf{A}_{2(b,:)}^T & \mathbf{A}_{3(c,:)}^T \end{bmatrix} \right). \quad (23)$$

As shown in [56], \mathbf{T} has no internal constraints and it can be estimated using 7 line correspondences.

Since \mathbf{T} is homogeneous, it has 7 DoF, matching the DoF of the canonical camera matrices. We verified that for every tensor $\mathbf{T} \in \mathbb{R}^{2 \times 2 \times 2}$, there are exactly two corresponding triplets of matrices $\mathbf{A}_{c,1}, \mathbf{A}_{c,2}, \mathbf{A}_{c,3}$. The proof and the decomposition algorithm for recovering these matrices can be found in the SM. Once $\mathbf{A}_{c,1}, \mathbf{A}_{c,2}, \mathbf{A}_{c,3}$ are found, we can triangulate the lines up to the projective transformation \mathbf{H} .

The solver for the $(B, 3, 7)$ problem, which estimates the trifocal tensor \mathbf{T} , operates as follows:

1. **Input:** Projections $\mathbf{p}_{i,j}$ of 7 lines in 3 cameras.

2. Compute matrices $\mathbf{R}_{0,i}$ and vectors $\mathbf{u}_{i,j}$ and $\mathbf{u}'_{i,j}$.
3. Construct the linear system (22).
4. Solve (22) using singular value decomposition (SVD) to estimate the tensor \mathbf{T} .

On average, the solver runs in 6.92 μs .

4.2. Vertical lines and known gravity

Here, we analyze the solutions to the problems $(E, 3, 5)$ and $(E, 4, 4)$. We assume that all lines are vertical and the gravity directions $\mathbf{v}_i \in \mathbb{P}^2$ for the cameras are known.

Similar to Sec. 4.1, we set $\mathbf{L}_{d,j} = \mathbf{e}_2$. Therefore, Equation (6) still holds. Furthermore the vanishing points \mathbf{v}_i for $i \in \{1, \dots, m\}$ associated with the vertical lines are known, and there holds $\mathbf{v}_i = \mathbf{R}_i(y_i)\mathbf{e}_2$. We can decompose $\mathbf{R}_i(y_i) = \mathbf{R}_{v,i}\mathbf{R}_{y,i}$, where $\mathbf{R}_{y,i}$ is a rotation around y-axis, and $\mathbf{R}_{v,i}$ is a rotation around an axis in the xz-plane, such that $\mathbf{R}_{v,i}\mathbf{e}_2 = \mathbf{v}_i$. Since $\mathbf{R}_{v,i}$ is calculated directly from \mathbf{v}_i , we assume it to be known.

In this case, \mathbf{R}'_i (5) takes the form $\mathbf{R}'_i = \mathbf{R}_{0,i}\mathbf{R}_{v,i}\mathbf{R}_{y,i}$. While both $\mathbf{R}_{0,i}$ and $\mathbf{R}_{v,i}$ have their axes in the xz-plane, $\mathbf{R}_{0,i}\mathbf{R}_{v,i}$ does generically not share this property. However, we can decompose $\mathbf{R}_{0,i}\mathbf{R}_{v,i} = \mathbf{R}_{a,i}\mathbf{R}_{b,i}$, s.t. $\mathbf{R}_{a,i}$ has its axis in the xz-plane and $\mathbf{R}_{b,i}$ rotates around the y-axis.

Now, we decompose \mathbf{R}'_i as $\mathbf{R}_{a,i} \cdot \mathbf{R}''_i$, where $\mathbf{R}_{a,i}$ is a known rotation around axis in the xz-plane, and $\mathbf{R}''_i = \mathbf{R}_{b,i} \cdot \mathbf{R}_{y,i}$ is an unknown rotation around y-axis.

We represent $\mathbf{R}_{a,i}, \mathbf{R}''_i$ with quaternions $\mathbf{q}_i = [\mathbf{q}_{i,w} \ \mathbf{q}_{i,x} \ 0 \ \mathbf{q}_{i,z}]^T$, $\mathbf{q}''_i = [\mathbf{q}''_{i,w} \ 0 \ \mathbf{q}''_{i,y} \ 0]^T$, write the elements of \mathbf{R}'_i in the form

$$\begin{aligned} \mathbf{R}'_{i(1,1)} &= (1 - 2\mathbf{q}_{i,z}^2)(1 - 2\mathbf{q}''_{i,y}) - 4\mathbf{q}_{i,x}\mathbf{q}_{i,z}\mathbf{q}''_{i,w}\mathbf{q}''_{i,y}, \\ \mathbf{R}'_{i(1,3)} &= 2(1 - 2\mathbf{q}_{i,z}^2)\mathbf{q}''_{i,w}\mathbf{q}''_{i,y} + 2\mathbf{q}_{i,x}\mathbf{q}_{i,z}(1 - 2\mathbf{q}''_{i,y}), \\ \mathbf{R}'_{i(3,1)} &= 2\mathbf{q}_{i,x}\mathbf{q}_{i,z}(1 - 2\mathbf{q}''_{i,y}) - 2(1 - 2\mathbf{q}_{i,x}^2)\mathbf{q}''_{i,w}\mathbf{q}''_{i,y}, \\ \mathbf{R}'_{i(3,3)} &= (1 - 2\mathbf{q}_{i,x}^2)(1 - 2\mathbf{q}''_{i,y}) + 4\mathbf{q}_{i,x}\mathbf{q}_{i,z}\mathbf{q}''_{i,w}\mathbf{q}''_{i,y}, \end{aligned} \quad (24)$$

and decompose the left 2×2 submatrix of \mathbf{A}_i (7) as

$$\begin{bmatrix} -\mathbf{R}'_{i(1,3)} & \mathbf{R}'_{i(1,1)} \\ -\mathbf{R}'_{i(3,3)} & \mathbf{R}'_{i(3,1)} \end{bmatrix} = \mathbf{A}_{i,a} \cdot \mathbf{A}_{i,b}, \quad (25)$$

with

$$\mathbf{A}_{i,a} = \begin{bmatrix} -2\mathbf{q}_{i,x}\mathbf{q}_{i,z} & (1 - 2\mathbf{q}_{i,z}^2) \\ -(1 - 2\mathbf{q}_{i,x}^2) & 2\mathbf{q}_{i,x}\mathbf{q}_{i,z} \end{bmatrix}, \quad (26)$$

$$\mathbf{A}_{i,b} = \begin{bmatrix} (1 - 2\mathbf{q}''_{i,y}) & 2\mathbf{q}''_{i,w}\mathbf{q}''_{i,y} \\ -2\mathbf{q}''_{i,w}\mathbf{q}''_{i,y} & (1 - 2\mathbf{q}''_{i,y}) \end{bmatrix}. \quad (27)$$

$\mathbf{A}_{i,a}$ can be directly obtained from the known gravity direction and the current scanline y_i , and $\mathbf{A}_{i,b}$ is an unknown $2D$ rotation matrix. We define $\mathbf{A}'_i = \mathbf{A}_{i,a}^{-1}\mathbf{A}_i$, and $\mathbf{u}''_{i,j} = \mathbf{A}'_{i,a}\mathbf{u}_{i,j}$. Then, there holds

$$\mathbf{u}''_{i,j}{}^T \mathbf{A}'_i \mathbf{L}_{j,h} = 0. \quad (28)$$

Since the left 2×2 submatrix of \mathbf{A}'_i is $\mathbf{A}_{i,b}$, \mathbf{A}'_i has a form of a calibrated 2×3 camera matrix, and the problem with known gravity direction and vertical lines is equivalent to estimating a 2D structure from images taken by n calibrated cameras [8]. Unlike its uncalibrated counterpart, the calibrated problem can be solved without projective ambiguity. Solvers for the cases $m = 3, n = 5$ and $m = 4, n = 4$ have been presented in [8]. Notably, these numbers exactly correspond to the minimal problems discussed in Sec. 3.

The solver for $m = 3, n = 5$ estimates a trifocal tensor of the form (23) from 5 point correspondences and 2 linear internal constraints, and solves a quadratic function to decompose the tensor into camera matrices. The solver for $m = 4, n = 4$ estimates a dual quadrifocal tensor from 4 point correspondences and 11 linear internal constraints, and also solves a quadratic function to decompose the tensor into camera matrices. In both cases, there are two solutions in terms of matrices \mathbf{A}'_i . Typically, the correct solution is selected by counting the points lying in front of all cameras.

After finding \mathbf{A}'_i with [8], we construct the camera poses $\mathbf{R}_i(y_i), \mathbf{C}_i(y_i)$. For this, we first obtain \mathbf{R}''_i . Because (28) is homogeneous, there are two possible matrices \mathbf{R}''_i :

$$\mathbf{R}''_i \in \left\{ \begin{array}{l} \left[\begin{array}{ccc} (1 - 2\mathbf{q}''_{i,y}) & 0 & 2\mathbf{q}''_{i,w}\mathbf{q}''_{i,y} \\ 0 & 1 & 0 \\ -2\mathbf{q}''_{i,w}\mathbf{q}''_{i,y} & 0 & (1 - 2\mathbf{q}''_{i,y}) \end{array} \right], \\ \left[\begin{array}{ccc} -(1 - 2\mathbf{q}''_{i,y}) & 0 & -2\mathbf{q}''_{i,w}\mathbf{q}''_{i,y} \\ 0 & 1 & 0 \\ 2\mathbf{q}''_{i,w}\mathbf{q}''_{i,y} & 0 & -(1 - 2\mathbf{q}''_{i,y}) \end{array} \right] \end{array} \right\}. \quad (29)$$

The existence of two choices of \mathbf{R}''_i per \mathbf{A}'_i accounts for the presence of 16 solutions in the 3 view case and 32 solutions in the 4 view case. Finally, we construct $\mathbf{R}_i(y_i), \mathbf{C}_i(y_i)$:

$$\begin{aligned} \mathbf{R}_i(y_i) &= \mathbf{R}_{0,i}^T \mathbf{R}_{a,i} \mathbf{R}''_i, \\ \mathbf{C}_i(y_i) &= [\mathbf{e}_1 \quad \mathbf{e}_3] \mathbf{A}_{i(1:2,1:2)}^{-1} \mathbf{A}_{i(1:2,3)}. \end{aligned} \quad (30)$$

Note, that $\mathbf{C}_i(y_i)_{(2)}$ is always zero. This is in accordance with the Section 2, which explains that the camera centers can only be estimated up to the shift along the direction \mathbf{L}_d .

To summarize, we perform the following steps to solve problems $(E, 3, 5)$ and $(E, 4, 4)$:

1. **Input:** Projections $\mathbf{p}_{i,j}$, vertical directions \mathbf{v}_i .
2. Calculate matrices $\mathbf{R}_{0,i}, \mathbf{R}_{v,i}, \mathbf{R}_{a,i}$, and vectors $\mathbf{u}_{i,j}$ (7).
3. Compose matrices $\mathbf{A}_{i,a}$ (26) and vectors $\mathbf{u}''_{i,j}$ (28).
4. Use the 3 view or the 4 view solver from [8] to find 2 sets of matrices $\mathbf{A}'_i, i \in \{1, \dots, m\}$ from $\mathbf{u}''_{i,j}$.
5. Construct \mathbf{R}''_i (29), $\mathbf{R}_i(y_i)$, and $\mathbf{C}_i(y_i)$ (30).

On average, the 3 view solver takes $9.16\mu s$, and the 4 view solver takes $70.84\mu s$.

4.3. Parallel lines and known gravity

We present the solution to the problem $(D, 3, 7)$. In this case, all lines share a common direction \mathbf{L}_d , which is

generically not aligned with the vertical direction \mathbf{e}_2 . Let $\mathbf{R}_d \in SO(3)$ be a rotation around an axis in the xz -plane, s.t. $\mathbf{L}_d = \mathbf{R}_d \mathbf{e}_2$. Substituting this into (3), we get

$$\mathbf{p}_{i,j}^T \mathbf{R}_i(y_i) [\mathbf{R}_d \mathbf{e}_2]_{\times} (\mathbf{L}_{0,j} - \mathbf{C}_i(y_i)) = 0, \quad (31)$$

$$\mathbf{p}_{i,j}^T \mathbf{R}_i(y_i) \mathbf{R}_d [\mathbf{e}_2]_{\times} \mathbf{R}_d^T (\mathbf{L}_{0,j} - \mathbf{C}_i(y_i)) = 0. \quad (32)$$

We define $\mathbf{L}'_{0,j} = \mathbf{R}_d^T \mathbf{L}_{0,j}$, $\mathbf{C}'_i = \mathbf{R}_d^T \mathbf{C}_i(y_i)$ and substitute these into (32):

$$\mathbf{p}_{i,j}^T \mathbf{R}_i(y_i) \mathbf{R}_d [\mathbf{e}_2]_{\times} (\mathbf{L}'_{0,j} - \mathbf{C}'_i) = 0. \quad (33)$$

Following Sec. 4.2, we find rotation matrices $\mathbf{R}_{0,i}$ and $\mathbf{R}_{v,i}$, decompose $\mathbf{R}_i(y_i)$ as $\mathbf{R}_{v,i} \mathbf{R}_{y,i}$, and find vectors $\mathbf{u}'_{i,j}$ according to (8). Then, we define $\mathbf{R}_{D,i} = \mathbf{R}_{0,i} \mathbf{R}_{v,i} \mathbf{R}_{y,i} \mathbf{R}_d$, and $\mathbf{t}_{D,i} = -\mathbf{R}_{D,i}^{-1} [\mathbf{e}_2]_{\times} \mathbf{C}'_i$, and rewrite the constraint as

$$\lambda_{i,j} \mathbf{u}'_{i,j} = \begin{bmatrix} -\mathbf{R}_{D,i(1,3)} & \mathbf{R}_{D,i(1,1)} & \mathbf{t}_{D,i(1)} \\ -\mathbf{R}_{D,i(3,3)} & \mathbf{R}_{D,i(3,1)} & \mathbf{t}_{D,i(3)} \end{bmatrix} \begin{bmatrix} \mathbf{L}'_{0,j(1)} \\ \mathbf{L}'_{0,j(3)} \\ 1 \end{bmatrix}, \quad (34)$$

which can be written in matrix form as

$$\lambda_{i,j} \mathbf{u}_{i,j} = \mathbf{A}_{D,i} \mathbf{L}'_{h,j}. \quad (35)$$

This equation has the same form as (8), ensuring the existence of a trifocal tensor $\mathbf{T} \in \mathbb{R}^{2,2,2}$ satisfying (22). We estimate this tensor linearly using 7 correspondences, as in Sec. 4.1.

Let us now discuss how to decompose \mathbf{T} to estimate the relative pose. First, we fix the coordinate frame by setting $\mathbf{R}_1(y_1) = I$, $\mathbf{C}_1(y_1) = 0$. Both the tensor \mathbf{T} and the pose have 7 DoF. Using Gröbner basis, we have discovered that for every tensor $\mathbf{T} \in \mathbb{R}^{2,2,2}$, there are 48 camera poses $\mathbf{R}_{y,2}, \mathbf{t}_{D,2}, \mathbf{R}_{y,3}, \mathbf{t}_{D,3}, \mathbf{R}_d$, such that the matrices $\mathbf{A}_{D,i}$ constructed via (34) have the tensor \mathbf{T} .

Due to the high number of variables and equation complexity, we could not generate an elimination template for a Gröbner basis solver. Therefore, we solve this problem with homotopy continuation [18], with an average runtime $19089\mu s$.

Finally, we compose $\mathbf{A}_{i,D}$ according to (34), and the pose $\mathbf{R}_i(y_i), \mathbf{C}_i(y_i)$ as

$$\begin{aligned} \mathbf{R}_i(y_i) &= \mathbf{R}_{v,i} \mathbf{R}_{y,i}, \\ \mathbf{C}_i(y_i) &= \mathbf{R}_d [\mathbf{e}_1 \quad \mathbf{e}_3] \mathbf{A}_{D,i(1:2,1:2)}^{-1} \mathbf{A}_{D,i(1:2,3)}. \end{aligned} \quad (36)$$

To summarize, we perform the following steps to solve the problem $(D, 3, 7)$:

1. **Input:** Projections $\mathbf{p}_{i,j}$, vertical directions \mathbf{v}_i .
2. Calculate matrices $\mathbf{R}_{0,i}, \mathbf{R}_{v,i}$ and vectors $\mathbf{u}_{i,j}$ (7).
3. Construct linear system (22) and solve it to get \mathbf{T} .
4. Use homotopy continuation to decompose \mathbf{T} into $\mathbf{R}_{y,2}, \mathbf{t}_{D,2}, \mathbf{R}_{y,3}, \mathbf{t}_{D,3}, \mathbf{R}_d$.
5. Construct $\mathbf{R}_i(y_i)$ and $\mathbf{C}_i(y_i)$ using (36).

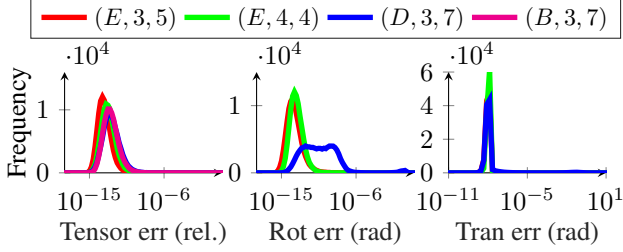


Figure 3. Histogram of tensor, rotation, and translation errors of the proposed solvers, over 10^5 noiseless samples. In radians.

4.4. Degenerate scenarios

Here, we analyze the degenerate cases for the solvers introduced in Sections 4.1, 4.2, and 4.3. Specifically, we consider scenarios where some lines are coplanar or where camera centers are collinear or coincident.

- Solvers $(E, 3, 5)$, $(E, 4, 4)$ are degenerate if all m lines are coplanar or if any two camera centers coincide.
- Solvers $(B, 3, 7)$, $(D, 3, 7)$ are degenerate if at least 5 lines are coplanar or if any two camera centers coincide.
- There is no degeneracy if the camera centers are collinear.

5. Experiments

In this section, we evaluate the solvers $(B, 3, 7)$, $(D, 3, 7)$, $(E, 3, 5)$, $(E, 4, 4)$ on both synthetic and real data.

5.1. Synthetic experiments

Numerical stability. We sample scanlines y_i from $\mathcal{U}_{[-1,1]}$ and generate random camera rotations $\mathbf{R}_{i,GT}$ and centers $\mathbf{C}_{i,GT}$. Since we use one scanline per image, we only sample one pose per image. We get the vertical directions as $v_i = \mathbf{R}_{i,GT} \mathbf{e}_2$. To generate line \mathbf{L}_j , we sample scalars $\mu_{j,x}, \mu_{j,z}$ from normalized Gaussian distribution and set $\mathbf{L}_{0,j} = [\mu_{j,x} \ 0 \ \mu_{j,z} + 5]^T$. For solver $(D, 3, 7)$, we also generate scalars ν_x, ν_z , and set $L_{j,d} = [\nu_x \ 1 \ \nu_z]^T$. In other cases, we use $L_{j,d} = \mathbf{e}_2$. We generate $\mathbf{p}_{i,j}$ by projecting \mathbf{L}_j into the camera with pose $(\mathbf{R}_{i,GT}, \mathbf{C}_{i,GT})$ and intersecting the projected line with scanline y_i .

Before measuring the error, we transform both the ground truth pose, and the estimated pose $(\mathbf{R}_{i,est}, \mathbf{C}_{i,est})$ into a canonical coordinate frame with $\mathbf{C}_1 = 0$, $\mathbf{R}_{y,1} = \mathbf{I}$, $\mathbf{L}_d = \mathbf{e}_1$. Since the y-coordinates of all camera centers are unobservable, we set them to zero. Then, we calculate the rotation error $err_{\mathbf{R}} = \max_{i=1}^m (\angle \mathbf{R}_{i,est}^T \mathbf{R}_{i,GT})$ and the translation error $err_{\mathbf{C}} = \max_{i=1}^m \angle(\mathbf{C}_{i,GT}, \mathbf{C}_{i,est})$.

Additionally, we construct tensors \mathbf{T}_{GT} from GT poses and estimate \mathbf{T}_{est} using the solvers. For trifocal problems, \mathbf{T}_{GT} , \mathbf{T}_{est} are trifocal tensors (23), while for $(E, 4, 4)$, they are dual quadrifocal tensors. We measure tensor error $err_{\mathbf{T}}$ as the Frobenius norm of $\mathbf{T}_{GT} - \mathbf{T}_{est}$. For each solver, we generate 10^5 synthetic noise-free scenes and measure $err_{\mathbf{R}}$, $err_{\mathbf{C}}$, and $err_{\mathbf{T}}$. Results in Fig. 3 show solver stability.

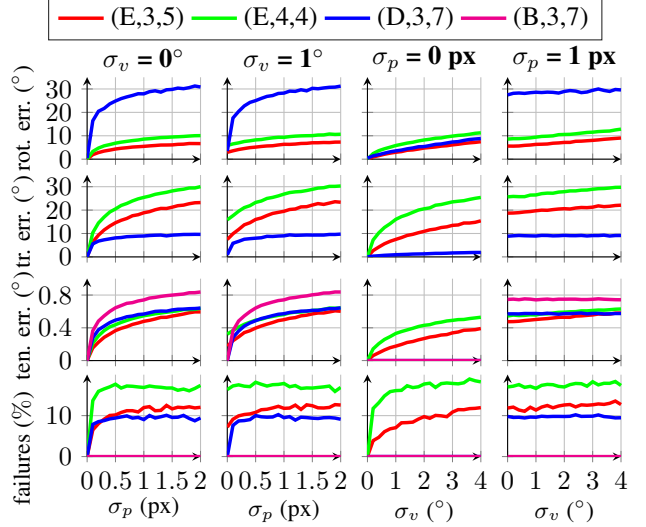


Figure 4. Rotation, translation, and tensor errors averaged over 10000 successful runs as a function of the point and the vertical noise, measured from the real solution closest to the ground truth. If a solver returns only complex solutions, we report a failure. The failure rates are reported in the last row. Plots in the same row share the y-axis and plots in the same column share the x-axis. The fixed parameters are in the titles.

Tests with noise. To evaluate the robustness to noise, we set focal length $f = 1000px$, and add Gaussian noise with standard deviation $\frac{\sigma_p}{f}$ to each projection $\mathbf{p}_{i,j}$. We also perturb vertical directions \mathbf{v}_i by applying a random 3D rotation with angle σ_v . Fig. 4 shows $err_{\mathbf{R}}$, $err_{\mathbf{C}}$, and $err_{\mathbf{T}}$ as the function of σ_p , σ_v , averaged over 10^4 runs. The results confirm that, since the line detections tend to be relatively precise, our solvers exhibit reasonable behaviour under realistic noise levels.

5.2. Real-world Experiments

We evaluate our solvers using the Fastec dataset [44], which consists of 19 sequences captured from a moving car in Tübingen. Each sequence contains 34 rolling shutter (RS) images and two global shutter (GS) images for every RS image: one with the pose of the first scanline and one with the pose of the middle scanline. The images have a resolution of 640×480 px and a focal length 768 px.

Since GT poses are unavailable, we use COLMAP [62] on the GS images to obtain pseudo-GT poses $(\mathbf{R}_{i,F}, \mathbf{C}_{i,F})$ for the first scanline of image i and $(\mathbf{R}_{i,M}, \mathbf{C}_{i,M})$ for the middle scanline. The pseudo-GT pose for scanline y_i is interpolated as: $\mathbf{R}_{i,GT}(y_i) = \mathbf{R}_{i,M \rightarrow y_i} \mathbf{R}_{i,M}$, $\mathbf{C}_{i,GT}(y_i) = \mathbf{C}_{i,M} + \frac{h-2y_i}{h} (\mathbf{C}_{i,F} - \mathbf{C}_{i,M})$, where $\mathbf{R}_{i,M \rightarrow y_i}$ is a rotation matrix with the axis of $\mathbf{R}_{i,F} \mathbf{R}_{i,M}^T$, and the angle $\frac{h-2y_i}{h}$ times the angle of $\mathbf{R}_{i,F} \mathbf{R}_{i,M}^T$. We evaluate the solvers in *multi-view* and *single-view* settings.

Multi-view. We estimate poses for m consecutive im-

	solver	$\leq 5^\circ$	$\leq 10^\circ$	$\leq 20^\circ$	$\leq 30^\circ$
MV	(E,3,5)	1	3	10	15
	(E,4,4)	5	8	11	14
	(D,3,7)	6	10	15	17
SV	(E,3,5)	3	3	5	10
	(E,4,4)	2	4	7	13
	(D,3,7)	4	4	7	9

Table 2. Number of sequences (out of 19) from the Fastec dataset [44], with at least one estimated pose with error below $5/10/20/30^\circ$. MV: *Multi-view*, SV: *Single-view*.

ages, selecting one scanline per image. We use DeepLSD [50] and Gluestick [51] to detect and match the lines. Although the projections of lines by RS cameras are generically curves, the line-based methods work well in the case of Fastec dataset. To select scanlines y_1, \dots, y_m , we exhaustively search for the scanlines that maximize the number of matched lines intersecting them. Then, we find $p_{i,j}$ as the intersections of the detected lines and the scanlines. Following [12], we approximate the vertical direction by $[0 \ 1 \ 0]^T$. This setting works well for many dataset, including Fastec, and does not require gravity direction measurement.

Single-view. In this case, select m scanlines in the same image and estimate the pose between them. We detect lines with DeepLSD [50], and select scanlines y_1, \dots, y_m with spacing at least 25px with the highest number of shared lines. We obtain $p_{i,j}$ by intersecting lines with scanlines.

We evaluate the solvers in RANSAC [22]. We label a correspondence as inlier, if the triangulated line L_j lies in front of all cameras and its reprojection error ε is below $1px$. In the case of $(B, 3, 7)$, we decompose the tensor into canonical cameras (20) before triangulation. Details about triangulation are in the SM. The score for a model is the sum over all lines of $(1px - \varepsilon)^2$ if $\varepsilon < 1px$, and zero otherwise. We run RANSAC for 1000 iterations, and select the model with the highest score. We do not use local optimization.

The results are summarized in Tables 2, 3 summarize the results for the solvers $(E, 3, 5)$, $(E, 4, 4)$, and $(D, 3, 7)$, and Table 4 shows the tensor error for the solver $(B, 3, 7)$. Although the total number of camera poses with an error below 10° and 20° remains relatively low, in Structure-from-Motion (SfM) applications, it is sufficient to estimate a single correct relative pose per sequence to initialize the reconstruction. Table 2 confirms that this is achievable for the vast majority of sequences. A more detailed evaluation and further experiments are provided in the SM.

6. Limitations and Future Work

While our approach shows promising results for rolling shutter relative pose estimation, several limitations remain. A key challenge is the lack of robust curve detectors and matchers, as rolling shutter distortion bends straight lines.

	solver	$\leq 10^\circ$	$\leq 20^\circ$	$\leq 30^\circ$
MV	(E,3,5)	1.0 %	6.2 %	21.9 %
	(E,4,4)	1.9 %	7.9 %	22.4 %
	(D,3,7)	5.6 %	13.8 %	21.7 %
SV	(E,3,5)	0.5 %	2.5 %	5.3 %
	(E,4,4)	1.2 %	4.1 %	10.0 %
	(D,3,7)	0.5 %	2.2 %	6.6 %

Table 3. Percentage of camera poses from Fastec [44] with pose error below $10/20/30^\circ$. MV: *Multi-view*, SV: *Single-view*.

setting	Median error	Minimum error
MV	0.85	0.44
SV	0.89	0.62

Table 4. Median and Minimum tensor error of the $(B, 3, 7)$ solver, averaged over all sequences from Fastec [44]. A more detailed evaluation is in the SM.

Additionally, our method relies on chirality constraints to resolve ambiguity, as noted in [8]. The method does not use any motion model, which makes it broadly applicable and model-agnostic. However, this universality comes at the cost of stability: we expect methods that incorporate motion models to be more stable. Our solvers are also limited to specific scene types and assumes a known gravity direction. However, this reliance could be mitigated using scene knowledge, such as geometric relations between lines, in combination with solver $(B, 3, 7)$. Finally, our method estimates pose only up to a shift along the line direction. Future work could integrate additional geometric constraints, improve feature detection, and integrate the solvers to a rolling-shutter SfM pipeline.

7. Conclusion

In this paper, we propose a new approach for estimating the relative pose of rolling shutter cameras using projections of lines onto multiple scanlines. This enables estimating relative pose of rolling shutter cameras without explicitly modelling camera motion. The proposed solvers provide an important building block for rolling-shutter SfM where each scanline has its pose computed independently, without relying on a global motion model.

We identify minimal problems for different variations of the single-scanline relative pose problem, including cases with parallel lines, vertical lines, and known gravity direction. Furthermore, we develop minimal solvers for the parallel-lines scenario, both with and without gravity priors. To evaluate our approach, we conduct experiments on both synthetic data and real-world rolling shutter images from the Fastec dataset, considering scanlines from either the same image or different images. These experiments demonstrate that our solvers successfully estimate at least one correct pose in the majority of scenes, confirming their feasibility for SfM initialization.

References

- [1] Omar Ait-Aider and François Berry. Structure and kinematics triangulation with a rolling shutter stereo rig. In *IEEE 12th International Conference on Computer Vision, ICCV 2009, Kyoto, Japan, September 27 - October 4, 2009*, 2009. 1
- [2] Omar Ait-Aider, Nicolas Andreff, Jean-Marc Lavest, and Philippe Martinet. Simultaneous object pose and velocity computation using a single view from a rolling shutter camera. In *Computer Vision - ECCV 2006, 9th European Conference on Computer Vision, Graz, Austria, May 7-13, 2006, Proceedings, Part II*, 2006. 1
- [3] Omar Ait-Aider, Adrien Bartoli, and Nicolas Andreff. Kinematics from lines in a single rolling shutter image. In *2007 IEEE Computer Society Conference on Computer Vision and Pattern Recognition (CVPR 2007), 18-23 June 2007, Minneapolis, Minnesota, USA, 2007*. 1
- [4] Cenek Albl, Zuzana Kukelova, and Tomás Pajdla. R6P - rolling shutter absolute pose problem. In *IEEE Conference on Computer Vision and Pattern Recognition, CVPR 2015, Boston, MA, USA, June 7-12, 2015*, 2015. 1
- [5] Cenek Albl, Zuzana Kukelova, and Tomás Pajdla. Rolling shutter absolute pose problem with known vertical direction. In *2016 IEEE Conference on Computer Vision and Pattern Recognition, CVPR 2016, Las Vegas, NV, USA, June 27-30, 2016*, 2016.
- [6] Cenek Albl, Zuzana Kukelova, Viktor Larsson, and Tomás Pajdla. Rolling shutter camera absolute pose. *IEEE Trans. Pattern Anal. Mach. Intell.*, 2020. 1
- [7] Cenek Albl, Zuzana Kukelova, Viktor Larsson, Michal Polic, Tomás Pajdla, and Konrad Schindler. From two rolling shutters to one global shutter. In *2020 IEEE/CVF Conference on Computer Vision and Pattern Recognition, CVPR 2020, Seattle, WA, USA, June 13-19, 2020*, 2020. 1
- [8] Kalle Åström and Magnus Oskarsson. Solutions and ambiguities of the structure and motion problem for 1d retinal vision. *J. Math. Imaging Vis.*, 2000. 2, 6, 8
- [9] Fang Bai, Agniva Sengupta, and Adrien Bartoli. Scanline homographies for rolling-shutter plane absolute pose. In *IEEE/CVF Conference on Computer Vision and Pattern Recognition, CVPR 2022, New Orleans, LA, USA, June 18-24, 2022*, 2022. 1, 2
- [10] Akash Bapat, Enrique Dunn, and Jan-Michael Frahm. Towards kilo-hertz 6-dof visual tracking using an egocentric cluster of rolling shutter cameras. *IEEE Trans. Vis. Comput. Graph.*, 2016. 2
- [11] Akash Bapat, True Price, and Jan-Michael Frahm. Rolling shutter and radial distortion are features for high frame rate multi-camera tracking. In *2018 IEEE Conference on Computer Vision and Pattern Recognition, CVPR 2018, Salt Lake City, UT, USA, June 18-22, 2018*, 2018. 2
- [12] Daniel Barath, Dmytro Mishkin, Luca Cavalli, Paul-Edouard Sarlin, Petr Hruby, and Marc Pollefeys. StereoGlue: Robust estimation with single-point solvers. In *Proceedings of the European Conference on Computer Vision (ECCV)*, 2024. 8
- [13] Paul Breiding and Sascha Timme. Homotopycontinuation.jl: A package for homotopy continuation in julia. In *Mathematical Software - ICMS 2018 - 6th International Conference, South Bend, IN, USA, July 24-27, 2018, Proceedings*. Springer, 2018. 3
- [14] Mingdeng Cao, Zhihang Zhong, Jiahao Wang, Yinqiang Zheng, and Yujiu Yang. Learning adaptive warping for real-world rolling shutter correction. *CoRR*, 2022. 1
- [15] Yuchao Dai, Hongdong Li, and Laurent Kneip. Rolling shutter camera relative pose: Generalized epipolar geometry. In *2016 IEEE Conference on Computer Vision and Pattern Recognition, CVPR 2016, Las Vegas, NV, USA, June 27-30, 2016*, 2016. 1
- [16] Juan Carlos Dibene, Yazmín Maldonado, Leonardo Trujillo, and Enrique Dunn. Prepare for ludicrous speed: Marker-based instantaneous binocular rolling shutter localization. *IEEE Trans. Vis. Comput. Graph.*, 2022. 2
- [17] Timothy Duff, Kathlén Kohn, Anton Leykin, and Tomás Pajdla. PLMP - point-line minimal problems in complete multi-view visibility. *IEEE Trans. Pattern Anal. Mach. Intell.*, 2024. 3
- [18] Ricardo Fabbri, Timothy Duff, Hongyi Fan, Margaret H. Regan, David da Costa de Pinho, Elias P. Tsigaridas, Charles W. Wampler, Jonathan D. Hauenstein, Peter J. Giblin, Benjamin B. Kimia, Anton Leykin, and Tomás Pajdla. TRPLP - trifocal relative pose from lines at points. In *2020 IEEE/CVF Conference on Computer Vision and Pattern Recognition, CVPR 2020, Seattle, WA, USA, June 13-19, 2020*, 2020. 6
- [19] Bin Fan, Yuchao Dai, and Ke Wang. Rolling-shutter-stereo-aware motion estimation and image correction. *Comput. Vis. Image Underst.*, 2021. 1
- [20] Bin Fan, Yuchao Dai, Zhiyuan Zhang, and Ke Wang. Differential sfm and image correction for a rolling shutter stereo rig. *Image Vis. Comput.*, 2022. 1
- [21] Bin Fan, Yuchao Dai, and Hongdong Li. Rolling shutter inversion: Bring rolling shutter images to high framerate global shutter video. *IEEE Trans. Pattern Anal. Mach. Intell.*, 2023. 1
- [22] Martin A. Fischler and Robert C. Bolles. Random sample consensus: a paradigm for model fitting with applications to image analysis and automated cartography. *Commun. ACM*, 1981. 8
- [23] Per-Erik Forssén and Erik Ringaby. Rectifying rolling shutter video from hand-held devices. In *The Twenty-Third IEEE Conference on Computer Vision and Pattern Recognition, CVPR 2010, San Francisco, CA, USA, 13-18 June 2010*, 2010. 1
- [24] Marvin Anas Hahn, Kathlén Kohn, Orlando Marigliano, and Tomás Pajdla. Order-one rolling shutter cameras. *CoRR*, 2024. 1
- [25] Radim Halir and Jan Flusser. Numerically stable direct least squares fitting of ellipses. In *Proc. 6th International Conference in Central Europe on Computer Graphics and Visualization. WSCG*, pages 125–132. Citeseer, 1998. 13
- [26] Michiel Hazewinkel. *Encyclopaedia of mathematics*. 2002. 1
- [27] Johan Hedberg, Erik Ringaby, Per-Erik Forssén, and Michael Felsberg. Structure and motion estimation from

- rolling shutter video. In *IEEE International Conference on Computer Vision Workshops, ICCV 2011 Workshops, Barcelona, Spain, November 6-13, 2011*, 2011. 1
- [28] Johan Hedborg, Per-Erik Forssén, Michael Felsberg, and Erik Ringaby. Rolling shutter bundle adjustment. In *2012 IEEE Conference on Computer Vision and Pattern Recognition, Providence, RI, USA, June 16-21, 2012*, 2012. 1
- [29] Radu Horaud, Roger Mohr, and Boguslaw Lorecki. On single-scanline camera calibration. *IEEE Trans. Robotics Autom.*, 1993. 2
- [30] Petr Hruby, Viktor Korotynskiy, Timothy Duff, Luke Oeding, Marc Pollefeys, Tomás Pajdla, and Viktor Larsson. Four-view geometry with unknown radial distortion. In *IEEE/CVF Conference on Computer Vision and Pattern Recognition, CVPR 2023, Vancouver, BC, Canada, June 17-24, 2023*, 2023. 5
- [31] Chao Jia and Brian L. Evans. Probabilistic 3-d motion estimation for rolling shutter video rectification from visual and inertial measurements. In *14th IEEE International Workshop on Multimedia Signal Processing, MMSP 2012, Banff, AB, Canada, September 17-19, 2012*, 2012. 1
- [32] Georg Klein and David William Murray. Parallel tracking and mapping on a camera phone. In *Science & Technology Proceedings, 8th IEEE International Symposium on Mixed and Augmented Reality 2009, ISMAR 2009, Orlando, Florida, USA, October 19-22, 2009*, 2009. 1
- [33] Zuzana Kukelova, Cenek Albl, Akihiro Sugimoto, and Tomás Pajdla. Linear solution to the minimal absolute pose rolling shutter problem. In *Computer Vision - ACCV 2018 - 14th Asian Conference on Computer Vision, Perth, Australia, December 2-6, 2018, Revised Selected Papers, Part III*, 2018. 1
- [34] Zuzana Kukelova, Cenek Albl, Akihiro Sugimoto, Konrad Schindler, and Tomás Pajdla. Minimal rolling shutter absolute pose with unknown focal length and radial distortion. In *Computer Vision - ECCV 2020 - 16th European Conference, Glasgow, UK, August 23-28, 2020, Proceedings, Part V*, 2020. 1
- [35] Yizhen Lao and Omar Ait-Aider. Rolling shutter homography and its applications. *IEEE Transactions on Pattern Analysis and Machine Intelligence*, 43(8):2780–2793, 2021. 1
- [36] Yizhen Lao, Omar Ait-Aider, and Helder Araújo. Robustified structure from motion with rolling-shutter camera using straightness constraint. *Pattern Recognit. Lett.*, 2018. 1
- [37] Yizhen Lao, Omar Ait-Aider, and Adrien Bartoli. Rolling shutter pose and ego-motion estimation using shape-from-template. In *Computer Vision - ECCV 2018 - 15th European Conference, Munich, Germany, September 8-14, 2018, Proceedings, Part II*, 2018. 1
- [38] Chang-Ryeol Lee and Kuk-Jin Yoon. Monocular visual odometry with a rolling shutter camera. *CoRR*, 2017. 1
- [39] Chang-Ryeol Lee and Kuk-Jin Yoon. Inertial-aided rolling shutter relative pose estimation. *CoRR*, 2017. 1
- [40] Chang-Ryeol Lee, Ju Hong Yoon, Min-Gyu Park, and Kuk-Jin Yoon. Gyroscope-aided relative pose estimation for rolling shutter cameras. *CoRR*, 2019. 1
- [41] Dongdong Li, Gongjian Wen, Bing Wei Hui, Shaohua Qiu, and Wenfei Wang. Cross-ratio invariant based line scan camera geometric calibration with static linear data. *Optics and Lasers in Engineering*, 2014. 2
- [42] Moyang Li, Peng Wang, Lingzhe Zhao, Bangyan Liao, and Peidong Liu. Usb-nerf: Unrolling shutter bundle adjusted neural radiance fields. In *The Twelfth International Conference on Learning Representations, ICLR 2024, Vienna, Austria, May 7-11, 2024*, 2024. 1
- [43] Bangyan Liao, Delin Qu, Yifei Xue, Huiqing Zhang, and Yizhen Lao. Revisiting rolling shutter bundle adjustment: Toward accurate and fast solution. In *IEEE/CVF Conference on Computer Vision and Pattern Recognition, CVPR 2023, Vancouver, BC, Canada, June 17-24, 2023*, 2023. 1
- [44] Peidong Liu, Zhaopeng Cui, Viktor Larsson, and Marc Pollefeys. Deep shutter unrolling network. In *Proc. IEEE Conf. on Computer Vision and Pattern Recognition (CVPR)*, 2020. 2, 7, 8, 13, 14, 15
- [45] Ludovic Magerand, Adrien Bartoli, Omar Ait-Aider, and Daniel Pizarro. Global optimization of object pose and motion from a single rolling shutter image with automatic 2d-3d matching. In *Computer Vision - ECCV 2012 - 12th European Conference on Computer Vision, Florence, Italy, October 7-13, 2012, Proceedings, Part I*, 2012. 1
- [46] Marci Meingast, Christopher Geyer, and Shankar Sasstry. Geometric models of rolling-shutter cameras. *CoRR*, abs/cs/0503076, 2005. 1
- [47] Branislav Micusik and Georgios Evangelidis. Renormalization for initialization of rolling shutter visual-inertial odometry. *Int. J. Comput. Vis.*, 2021. 1
- [48] Thanh-Tin Nguyen and Maxime Lhuillier. Adding synchronization and rolling shutter in multi-camera bundle adjustment. In *Proceedings of the British Machine Vision Conference 2016, BMVC 2016, York, UK, September 19-22, 2016*, 2016. 1
- [49] David Nistér. An efficient solution to the five-point relative pose problem. *IEEE Trans. Pattern Anal. Mach. Intell.*, 2004. 1, 13
- [50] Rémi Pautrat, Daniel Barath, Viktor Larsson, Martin R. Oswald, and Marc Pollefeys. Deepplsd: Line segment detection and refinement with deep image gradients. In *Computer Vision and Pattern Recognition (CVPR)*, 2023. 8
- [51] Rémi* Pautrat, Iago* Suárez, Yifan Yu, Marc Pollefeys, and Viktor Larsson. GlueStick: Robust image matching by sticking points and lines together. In *International Conference on Computer Vision (ICCV)*, 2023. 8
- [52] Pulak Purkait and Christopher Zach. Minimal solvers for monocular rolling shutter compensation under ackermann motion. In *2018 IEEE Winter Conference on Applications of Computer Vision, WACV 2018, Lake Tahoe, NV, USA, March 12-15, 2018*, 2018. 1
- [53] Pulak Purkait, Christopher Zach, and Ales Leonardis. Rolling shutter correction in manhattan world. In *IEEE International Conference on Computer Vision, ICCV 2017, Venice, Italy, October 22-29, 2017*, 2017. 1
- [54] Delin Qu, Yizhen Lao, Zhigang Wang, Dong Wang, Bin Zhao, and Xuelong Li. Towards nonlinear-motion-aware and

- occlusion-robust rolling shutter correction. In *IEEE/CVF International Conference on Computer Vision, ICCV 2023, Paris, France, October 1-6, 2023*, 2023. 1
- [55] Delin Qu, Bangyan Liao, Huiqing Zhang, Omar Ait-Aider, and Yizhen Lao. Fast rolling shutter correction in the wild. *IEEE Trans. Pattern Anal. Mach. Intell.*, 2023. 1
- [56] Long Quan and Takeo Kanade. Affine structure from line correspondences with uncalibrated affine cameras. *IEEE Trans. Pattern Anal. Mach. Intell.*, 1997. 2, 3, 5
- [57] Vijay Rengarajan, A. N. Rajagopalan, and Rangarajan Aravind. From bows to arrows: Rolling shutter rectification of urban scenes. In *2016 IEEE Conference on Computer Vision and Pattern Recognition, CVPR 2016, Las Vegas, NV, USA, June 27-30, 2016*, 2016. 1
- [58] Erik Ringaby and Per-Erik Forssén. Efficient video rectification and stabilisation for cell-phones. *Int. J. Comput. Vis.*, 2012. 1
- [59] Olivier Saurer, Kevin Köser, Jean-Yves Bouguet, and Marc Pollefeys. Rolling shutter stereo. In *IEEE International Conference on Computer Vision, ICCV 2013, Sydney, Australia, December 1-8, 2013*, 2013. 1
- [60] Olivier Saurer, Marc Pollefeys, and Gim Hee Lee. A minimal solution to the rolling shutter pose estimation problem. In *2015 IEEE/RSJ International Conference on Intelligent Robots and Systems, IROS 2015, Hamburg, Germany, September 28 - October 2, 2015*, 2015. 1
- [61] Olivier Saurer, Marc Pollefeys, and Gim Hee Lee. Sparse to dense 3d reconstruction from rolling shutter images. In *2016 IEEE Conference on Computer Vision and Pattern Recognition, CVPR 2016, Las Vegas, NV, USA, June 27-30, 2016*, 2016. 1
- [62] Johannes Lutz Schönberger and Jan-Michael Frahm. Structure-from-motion revisited. In *Conference on Computer Vision and Pattern Recognition (CVPR)*, 2016. 1, 7, 13
- [63] David Schubert, Nikolaus Demmel, Vladyslav Usenko, Jörg Stückler, and Daniel Cremers. Direct sparse odometry with rolling shutter. In *Computer Vision - ECCV 2018 - 15th European Conference, Munich, Germany, September 8-14, 2018, Proceedings, Part VIII*, 2018. 1
- [64] Wei Shang, Dongwei Ren, Chaoyu Feng, Xiaotao Wang, Lei Lei, and Wangmeng Zuo. Self-supervised learning to bring dual reversed rolling shutter images alive. In *IEEE/CVF International Conference on Computer Vision, ICCV 2023, Paris, France, October 1-6, 2023*, 2023. 1
- [65] Ken Shoemake. Animating rotation with quaternion curves. In *SIGGRAPH*, 1985. 1
- [66] Henrik Stewénus, David Nistér, Magnus Oskarsson, and Kalle Åström. Solutions to minimal generalized relative pose problems. *Workshop on omnidirectional vision*, 2005. 2
- [67] Daobilige Su, Asher Bender, and Salah Sukkarieh. Improved cross-ratio invariant-based intrinsic calibration of A hyper-spectral line-scan camera. *Sensors*, 2018. 2
- [68] Jiaming Sun, Zehong Shen, Yuang Wang, Hujun Bao, and Xiaowei Zhou. Loftr: Detector-free local feature matching with transformers. In *Proceedings of the IEEE/CVF conference on computer vision and pattern recognition*, pages 8922–8931, 2021. 13
- [69] Yufen Sun, Gang Liu, and Yue Sun. An affine motion model for removing rolling shutter distortions. *IEEE Signal Process. Lett.*, 2016. 1
- [70] Subeesh Vasu, Mahesh Mohan M. R., and A. N. Rajagopalan. Occlusion-aware rolling shutter rectification of 3d scenes. In *2018 IEEE Conference on Computer Vision and Pattern Recognition, CVPR 2018, Salt Lake City, UT, USA, June 18-22, 2018*, 2018. 1
- [71] Carlos Andrés Luna Vázquez, Manuel Mazo, José Luis Lázaro, and Juan F. Vazquez. Calibration of line-scan cameras. *IEEE Trans. Instrum. Meas.*, 2010. 2
- [72] Ke Wang, Bin Fan, and Yuchao Dai. Relative pose estimation for stereo rolling shutter cameras. In *IEEE International Conference on Image Processing, ICIP 2020, Abu Dhabi, United Arab Emirates, October 25-28, 2020*, 2020. 1
- [73] Bo Xu, Ziao Liu, Mengqi Guo, Jiancheng Li, and Gim Hee Lee. Urs-nerf: Unordered rolling shutter bundle adjustment for neural radiance fields. In *Computer Vision - ECCV 2024 - 18th European Conference, Milan, Italy, September 29-October 4, 2024, Proceedings, Part XXXV*, 2024. 1
- [74] Weilong Yan, Robby T. Tan, Bing Zeng, and Shuaicheng Liu. Deep homography mixture for single image rolling shutter correction. In *IEEE/CVF International Conference on Computer Vision, ICCV 2023, Paris, France, October 1-6, 2023*, 2023. 1
- [75] Ming Yao, Zuyun Zhao, and Bugao Xu. Geometric calibration of line-scan camera using a planar pattern. *J. Electronic Imaging*, 2014. 2
- [76] Yongcong Zhang, Bangyan Liao, Yifei Xue, Chen Lu, Peidong Liu, and Yizhen Lao. RSL-BA: rolling shutter line bundle adjustment. In *Computer Vision - ECCV 2024 - 18th European Conference, Milan, Italy, September 29-October 4, 2024, Proceedings, Part LIX*, 2024. 1
- [77] Bingbing Zhuang and Quoc-Huy Tran. Image stitching and rectification for hand-held cameras. In *Computer Vision - ECCV 2020 - 16th European Conference, Glasgow, UK, August 23-28, 2020, Proceedings, Part VII*, 2020. 1
- [78] Bingbing Zhuang, Loong-Fah Cheong, and Gim Hee Lee. Rolling-shutter-aware differential sfm and image rectification. In *IEEE International Conference on Computer Vision, ICCV 2017, Venice, Italy, October 22-29, 2017*, 2017. 1
- [79] Bingbing Zhuang, Quoc-Huy Tran, Pan Ji, Loong-Fah Cheong, and Manmohan Chandraker. Learning structure-and-motion-aware rolling shutter correction. In *IEEE Conference on Computer Vision and Pattern Recognition, CVPR 2019, Long Beach, CA, USA, June 16-20, 2019*, 2019. 1

Single-Scanline Relative Pose Estimation for Rolling Shutter Cameras

Supplementary Material

A. Decomposition of the Trifocal Tensor into Canonical Cameras

Given a trifocal tensor $\mathbf{T} \in \mathbb{R}^{2,2,2}$, we describe that we can decompose it into two possible sets of 2×3 matrices ($\mathbf{A}_{c,1}, \mathbf{A}_{c,2}, \mathbf{A}_{c,3}$) in the canonical form, described in Eq. (20) of the main paper.

First, we note that calculating the tensor elements according to Eq. (23) of the main paper from cameras $\mathbf{A}_{c,1}, \mathbf{A}_{c,2}, \mathbf{A}_{c,3}$ yields

- $T_{000} = 1$
- $T_{001} = \alpha_7$
- $T_{010} = \alpha_3$
- $T_{011} = \alpha_3\alpha_7 - \alpha_4\alpha_6$
- $T_{100} = \alpha_1$
- $T_{010} = \alpha_1\alpha_7 - \alpha_1\alpha_5$
- $T_{110} = \alpha_1\alpha_3 - \alpha_1\alpha_2$
- $T_{111} = \alpha_1\alpha_3\alpha_7 - \alpha_1\alpha_4\alpha_6 - \alpha_1\alpha_2\alpha_7 + \alpha_1\alpha_4\alpha_5 + \alpha_1\alpha_2\alpha_6 - \alpha_1\alpha_3\alpha_5$

We normalize the tensor such that its first entry is 1:

$$\mathbf{T} \leftarrow \frac{\mathbf{T}}{T_{000}}. \quad (37)$$

From the normalized tensor, we extract the parameters:

$$\begin{aligned} \alpha_1 &= T_{100}, & \alpha_3 &= T_{010}, & \alpha_7 &= T_{001}, \\ \alpha_5 &= \frac{-T_{101} + \alpha_1\alpha_7}{\alpha_1}, & \alpha_2 &= \frac{-T_{110} + \alpha_1\alpha_3}{\alpha_1}. \end{aligned} \quad (39)$$

Now, T_{100} and T_{111} give two constraints for α_4, α_6 . In the equation for T_{111} , we substitute $\alpha_3\alpha_7 - T_{100}$ to get a linear constraint in α_4, α_6 . Expressing α_6 from this constraint and substituting into the constraint for T_{100} yields a quadratic equation

$$c_A\alpha_4^2 + c_B\alpha_4 + c_C = 0 \quad (40)$$

with coefficients

$$\begin{aligned} c_A &= -\frac{\alpha_5}{\alpha_2}, \\ c_B &= \frac{T_{111} - \alpha_1\alpha_3\alpha_7 + \alpha_1(\alpha_3\alpha_7 - T_{011}) + \alpha_1\alpha_2\alpha_7 + \alpha_1\alpha_3\alpha_5}{\alpha_1\alpha_2}, \\ c_C &= T_{011} - \alpha_3\alpha_7. \end{aligned} \quad (41)$$

Solving (40), we obtain two solutions:

$$\begin{aligned} \alpha_{4a} &= \frac{-c_B + \sqrt{c_B^2 - 4c_Ac_C}}{2c_A}, \\ \alpha_{4b} &= \frac{-c_B - \sqrt{c_B^2 - 4c_Ac_C}}{2c_A}. \end{aligned} \quad (42)$$

Finally, we find the corresponding values α_{6a}, α_{6b} of α_6 from the equation for T_{111} .

Using these values, we construct two sets of projection matrices:

$$\mathbf{A}_1 = \begin{bmatrix} 1 & 0 & 0 \\ \alpha_1 & \alpha_1 & \alpha_1 \end{bmatrix}, \quad (43)$$

$$\mathbf{A}_2 = \begin{bmatrix} 0 & 1 & 0 \\ \alpha_2 & \alpha_3 & \alpha_4 \end{bmatrix}, \quad (44)$$

$$\mathbf{A}_3 = \begin{bmatrix} 0 & 0 & 1 \\ \alpha_5 & \alpha_6 & \alpha_7 \end{bmatrix}, \quad (45)$$

where (α_4, α_6) takes either $(\alpha_{4a}, \alpha_{6a})$ or $(\alpha_{4b}, \alpha_{6b})$, yielding two valid decompositions.

This method provides a direct way to extract the projection matrices from a given trifocal tensor while preserving the canonical structure. This also shows, that for a generic tensor $\mathbf{T} \in \mathbb{R}^{2,2,2}$ there are two ways to decompose it into matrices in the canonical form.

B. Triangulation of Lines from a Single Scanline

Given the projections of a 3D line onto a single scanline, we describe how we estimate a point \mathbf{L}_0 on the line and measure the reprojection error. Since the line direction \mathbf{L}_d is known and corresponds to the y-axis, the problem reduces to estimating the 3D position of one point \mathbf{L}_0 on the line. Let $\mathbf{A}_i \in \mathbb{R}^{2 \times 3}$ be the projection matrix encoding the pose of the i -th camera, and let $\mathbf{u}_i \in \mathbb{R}^2$ be the measured projection of the line on the scanline. We construct the constraint matrix $\mathbf{M} \in \mathbb{R}^{m \times 3}$ as:

$$\mathbf{M} = \begin{bmatrix} \frac{\mathbf{u}_1^T \mathbf{A}_1}{\|\mathbf{u}_1^T \mathbf{A}_1\|} \\ \dots \\ \frac{\mathbf{u}_m^T \mathbf{A}_m}{\|\mathbf{u}_m^T \mathbf{A}_m\|} \end{bmatrix}. \quad (46)$$

We solve for the homogeneous line representation \mathbf{L}_h as the right singular vector corresponding to the smallest singular value of \mathbf{M} :

$$\mathbf{L}_h = \arg \min_{\|\mathbf{L}\|=1} \|\mathbf{M}\mathbf{L}\|. \quad (47)$$

Normalizing \mathbf{L}_h such that its third component is 1, we obtain:

$$\mathbf{L}_h = \frac{\mathbf{L}_h}{L_{h(3)}}. \quad (48)$$

The estimated 3D point on the line is then given by:

$$\mathbf{L}_0 = \begin{bmatrix} \mathbf{L}_{h(1)} \\ 0 \\ \mathbf{L}_{h(2)} \end{bmatrix}. \quad (49)$$

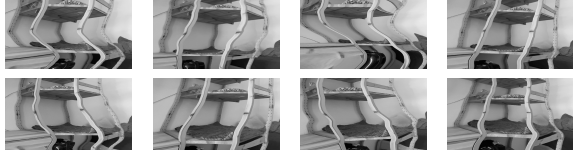


Figure 5. Custom images used in the experiment in Section C.2.

To evaluate the reprojection error, we compute the projected coordinates of \mathbf{L}_h :

$$\mathbf{p}_i = \mathbf{A}_i \mathbf{L}_h, \quad (50)$$

and measure the angular deviation from the observed scanline projection:

$$e_i = \left| \frac{p_{i,2}}{p_{i,1}} + \frac{u_{i,0}}{u_{i,1}} \right|. \quad (51)$$

We get the total reprojection error by:

$$e_{\text{total}} = \sum_{i=1}^m e_i^2. \quad (52)$$

C. Additional experiments

C.1. Detailed evaluation of the experiments from the main paper

Here, we present detailed results of the experiments conducted on the real-world dataset Fastec [44]. In the case of solvers $(E, 3, 5)$, $(E, 4, 4)$, and $(D, 3, 7)$, we present median and minimum rotation and translation errors for every sequence from the Fastec dataset, as well as the percentages of scenes, whose pose error (obtained as the maximum over the rotation and translation error) does not exceed 10° , 20° , and 30° . In the case of solver $(B, 3, 7)$, we cannot measure the pose error, so we present the median and minimum tensor error for every sequence from the Fastec dataset.

C.2. Evaluation on images with very large rolling-shutter distortions

Here, we present an evaluation of our method on a custom dataset simulated very large rolling-shutter distortions. This scenario, while not very realistic, demonstrates that the proposed solvers are not limited to a particular type of motion. We have taken multiple high speed videos of the same scene with an iPhone, and simulated rolling shutter images (Fig. 5) by selecting one scanline per frame. We have generated ground truth poses for every frame and obtained the camera intrinsics using COLMAP [62].

While it is very difficult to detect the whole lines, our method only needs to detect the segment of the line in the vicinity of a selected scanline. To detect these, we have found Canny edges in the images, and fitted conics into the edge points using [25]. To match the curves, we obtained

Seq	R,t errors in $^\circ$				Percentage of errors below $10^\circ / 20^\circ / 30^\circ$
	Median	Minimum	Minimum	Minimum	
4	1.0	71.8	6.0	12.0	0.0 / 18.5 / 33.3
9	4.0	45.3	2.6	16.9	0.0 / 3.2 / 9.7
10	3.8	40.5	0.9	16.2	0.0 / 9.4 / 34.4
11	2.7	32.1	0.2	8.9	3.1 / 21.9 / 40.6
13	3.2	38.1	0.9	7.5	3.1 / 12.5 / 12.5
16	4.1	42.4	3.1	32.7	0.0 / 0.0 / 0.0
17	2.0	38.6	1.0	13.8	0.0 / 12.5 / 31.3
18	6.0	44.7	2.2	20.3	0.0 / 0.0 / 25.0
20	2.4	42.8	1.0	20.0	0.0 / 0.0 / 31.3
21	2.8	63.8	6.3	32.6	0.0 / 0.0 / 0.0
32	3.8	43.6	11.1	26.3	0.0 / 0.0 / 8.0
50	0.6	34.3	0.1	20.1	0.0 / 0.0 / 37.5
64	1.9	71.2	0.5	10.8	0.0 / 4.5 / 4.5
74	1.9	118.8	1.9	115.8	0.0 / 0.0 / 0.0
76	0.8	111.4	0.3	51.3	0.0 / 0.0 / 0.0
79	1.4	25.2	0.4	10.7	0.0 / 15.6 / 62.5
88	3.4	40.0	1.8	27.1	0.0 / 0.0 / 10.0
92	2.2	25.9	0.6	3.3	12.5 / 12.5 / 59.4
100	4.0	44.3	7.6	19.0	0.0 / 6.3 / 15.6

Table 5. Detailed evaluation of the errors for solver $(E, 3, 5)$ in the multi-view setting. For every sequence of Fastec [44], we give the median and the minimum rotation and translation error, as well as the percentage of pose errors below 10° , 20° , 30° .

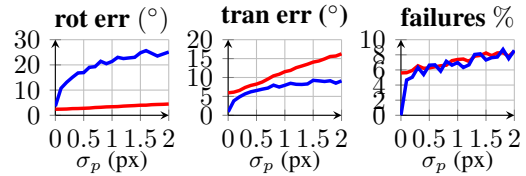


Figure 6. Synthetic tests for solvers $(E, 3, 5)$ and $(D, 3, 7)$ with local optimization using 10 lines. $\sigma_v = 1^\circ$.

point matches using LoFTR [68], associated every detected curve with keypoints within 2px from it, and used the number of shared associated keypoints as the score for matching the curves.

We estimated the pose for every camera triplet from Fig. 5 using solver $(E, 3, 5)$. The median rotation and translation error are 4.8° and 14.8° . 30.6% triplets have pose error below 10° , and 56.5% have pose error below 20° . Every image is in at least one triplet with pose error below 6° .

We have further evaluated the five point solver [49] on all images pairs from Fig. 5. The median rotation and translation error are 6.6° and 44.4° . 10.7% triplets have pose error below 10° , and 21.4% have pose error below 20° . This demonstrates that our method can handle large rolling-shutter distortions better than the five point solver.

Seq	R,t errors in $^{\circ}$				Percentage of errors below $10^{\circ} / 20^{\circ} / 30^{\circ}$
	Median		Minimum		
4	1.8	112.4	0.4	4.6	4.3 / 17.4 / 26.1
9	5.3	43.8	1.1	10.6	0.0 / 10.0 / 16.7
10	3.1	27.0	0.7	2.4	3.2 / 22.6 / 58.1
11	3.8	36.1	3.8	7.8	3.2 / 22.6 / 35.5
13	3.5	36.8	1.7	2.6	6.5 / 19.4 / 35.5
16	6.9	50.5	3.7	32.3	0.0 / 0.0 / 0.0
17	2.8	40.4	1.2	3.4	3.2 / 6.5 / 25.8
18	7.0	71.3	4.5	36.5	0.0 / 0.0 / 0.0
20	2.8	35.7	0.6	12.4	0.0 / 16.1 / 32.3
21	5.2	70.4	3.0	9.4	3.2 / 3.2 / 3.2
32	5.5	54.3	19.5	27.8	0.0 / 0.0 / 5.3
50	2.2	62.4	1.1	17.9	0.0 / 6.5 / 22.6
64	1.4	82.2	2.0	30.6	0.0 / 0.0 / 0.0
74	5.1	115.5	5.1	115.5	0.0 / 0.0 / 0.0
76	3.1	128.4	3.5	110.6	0.0 / 0.0 / 0.0
79	2.3	43.0	0.7	21.7	0.0 / 0.0 / 20.7
88	3.5	28.2	4.3	21.7	0.0 / 0.0 / 66.7
92	4.6	26.4	2.3	4.0	9.7 / 22.6 / 54.8
100	3.8	42.8	0.9	6.5	3.2 / 3.2 / 22.6

Table 6. Detailed evaluation of the errors for solver ($E, 4, 4$) in the multi-view setting. For every sequence of Fastec [44], we give the median and the minimum rotation and translation error, as well as the percentage of pose errors below $10^{\circ}, 20^{\circ}, 30^{\circ}$.

C.3. Pose estimation with local optimization

We have added local optimization (LO) after the solvers ($E, 3, 5$) and ($D, 3, 7$), and evaluated them on synthetic and real data. The result on synthetic data with 10 lines per scene (Fig. 6) shows that the LO improves the pose. However, the effect of the local optimization on real data from the Fastec dataset and from Fig. 5 is marginal, mostly due to a low number of lines in the images.

Seq	R,t errors in $^{\circ}$				Percentage of errors below $10^{\circ} / 20^{\circ} / 30^{\circ}$
	Median		Minimum		
4	1.6	83.3	0.9	14.4	0.0 / 7.4 / 14.8
9	8.6	55.0	16.8	24.6	0.0 / 0.0 / 3.2
10	6.1	49.3	2.5	1.2	6.3 / 18.8 / 21.9
11	10.4	59.7	2.1	7.3	6.5 / 22.6 / 25.8
13	5.1	41.0	0.4	8.6	3.1 / 18.8 / 40.6
16	13.0	57.7	6.2	35.4	0.0 / 0.0 / 0.0
17	3.8	37.2	2.4	3.2	9.4 / 21.9 / 46.9
18	8.1	93.5	3.0	24.2	0.0 / 0.0 / 16.7
20	4.2	57.0	1.9	10.4	0.0 / 9.4 / 18.8
21	6.3	85.8	4.2	4.8	3.1 / 9.4 / 12.5
32	6.4	85.6	2.4	1.1	16.0 / 24.0 / 36.0
50	3.2	94.7	1.5	12.5	0.0 / 3.1 / 9.4
64	31.7	153.4	2.0	17.9	0.0 / 4.3 / 4.3
74	180.0	180.0	180.0	180.0	0.0 / 0.0 / 0.0
76	5.7	141.3	4.4	10.4	0.0 / 5.0 / 10.0
79	6.1	44.8	2.1	2.8	3.1 / 15.6 / 28.1
88	3.1	10.0	3.0	2.7	50.0 / 70.0 / 80.0
92	6.8	53.8	6.5	9.7	6.3 / 25.0 / 28.1
100	8.0	54.0	1.0	8.5	3.1 / 6.3 / 15.6

Table 7. Detailed evaluation of the errors for solver ($D, 3, 7$) in the multi-view setting. For every sequence of Fastec [44], we give the median and the minimum rotation and translation error, as well as the percentage of pose errors below $10^{\circ}, 20^{\circ}, 30^{\circ}$.

Seq	R,t errors in $^{\circ}$				Percentage of errors below $10^{\circ} / 20^{\circ} / 30^{\circ}$
	Median		Minimum		
4	4.7	55.8	0.3	29.9	0.00 / 0.00 / 2.94
9	0.5	117.8	0.5	2.6	3.03 / 3.03 / 6.06
10	0.4	49.7	0.4	20.0	0.00 / 2.94 / 2.94
11	1.3	52.2	3.0	12.0	0.00 / 5.88 / 5.88
13	0.5	93.8	0.1	36.3	0.00 / 0.00 / 0.00
16	7.1	129.6	0.2	28.1	0.00 / 0.00 / 4.00
17	1.7	51.7	0.3	43.2	0.00 / 0.00 / 0.00
18	89.9	128.7	5.2	41.8	0.00 / 0.00 / 0.00
20	0.3	51.0	0.6	1.2	2.94 / 2.94 / 11.76
21	0.3	29.2	0.2	4.3	2.94 / 32.35 / 52.94
32	3.2	130.1	3.9	46.9	0.00 / 0.00 / 0.00
50	4.4	125.9	1.2	47.7	0.00 / 0.00 / 0.00
64	90.1	136.2	8.4	48.1	0.00 / 0.00 / 0.00
74	179.9	179.9	179.9	179.9	0.00 / 0.00 / 0.00
76	47.6	133.9	0.2	24.8	0.00 / 0.00 / 5.00
79	0.7	115.5	8.1	23.9	0.00 / 0.00 / 2.94
88	10.8	55.3	0.1	46.7	0.00 / 0.00 / 0.00
92	0.7	133.3	0.3	37.6	0.00 / 0.00 / 0.00
100	0.4	96.2	2.7	21.3	0.00 / 0.00 / 5.88

Table 8. Detailed evaluation of the errors for solver ($E, 3, 5$) in the single-view setting. For every sequence of Fastec [44], we give the median and the minimum rotation and translation error, as well as the percentage of pose errors below $10^{\circ}, 20^{\circ}, 30^{\circ}$.

Seq	R,t errors in $^{\circ}$				Percentage of errors below $10^{\circ} / 20^{\circ} / 30^{\circ}$
	Median		Minimum		
4	1.4	81.2	1.7	1.5	11.11 / 18.52 / 22.22
9	0.3	86.7	0.2	22.7	0.00 / 0.00 / 6.06
10	0.3	49.8	1.2	6.0	3.03 / 9.09 / 15.15
11	0.9	77.1	0.3	10.2	0.00 / 8.82 / 11.76
13	0.6	111.6	0.0	51.5	0.00 / 0.00 / 0.00
16	0.1	57.5	0.1	23.0	0.00 / 0.00 / 7.69
17	0.7	71.0	0.5	3.0	5.88 / 14.71 / 17.65
18	0.5	127.4	8.5	20.1	0.00 / 0.00 / 12.50
20	0.3	59.5	0.7	11.6	0.00 / 11.76 / 17.65
21	0.2	35.4	0.3	15.4	0.00 / 11.76 / 47.06
32	0.3	49.8	1.7	22.2	0.00 / 0.00 / 10.53
50	0.0	125.2	11.3	68.9	0.00 / 0.00 / 0.00
64	1.3	134.6	3.7	27.0	0.00 / 0.00 / 7.69
74	179.9	179.9	179.9	179.9	0.00 / 0.00 / 0.00
76	0.3	74.0	1.0	26.8	0.00 / 0.00 / 11.11
79	0.3	121.5	0.1	38.8	0.00 / 0.00 / 0.00
88	0.0	47.5	0.0	46.6	0.00 / 0.00 / 0.00
92	0.1	47.2	0.1	42.0	0.00 / 0.00 / 0.00
100	0.2	87.3	0.4	5.2	2.94 / 2.94 / 2.94

Table 9. Detailed evaluation of the errors for solver ($E, 4, 4$) in the single-view setting. For every sequence of Fastec [44], we give the median and the minimum rotation and translation error, as well as the percentage of pose errors below 10° , 20° , 30° .

Seq	R,t errors in $^{\circ}$				Percentage of errors below $10^{\circ} / 20^{\circ} / 30^{\circ}$
	Median		Minimum		
4	1.8	48.5	32.4	43.2	0.00 / 0.00 / 0.00
9	0.2	52.9	1.5	3.9	3.03 / 6.06 / 15.15
10	2.1	48.0	25.3	36.0	0.00 / 0.00 / 0.00
11	7.6	48.4	1.1	17.6	0.00 / 2.94 / 5.88
13	3.2	55.9	0.1	24.8	0.00 / 0.00 / 14.71
16	2.7	50.1	14.6	43.4	0.00 / 0.00 / 0.00
17	2.2	49.7	22.8	36.5	0.00 / 0.00 / 0.00
18	6.9	56.8	6.6	26.2	0.00 / 0.00 / 4.17
20	3.2	48.5	18.0	3.1	0.00 / 2.94 / 8.82
21	1.5	28.4	2.1	3.0	2.94 / 20.59 / 61.76
32	1.5	48.8	26.2	33.3	0.00 / 0.00 / 0.00
50	10.3	60.5	4.4	49.9	0.00 / 0.00 / 0.00
64	3.2	44.2	5.4	39.8	0.00 / 0.00 / 0.00
74	180.0	180.0	180.0	180.0	0.00 / 0.00 / 0.00
76	2.2	45.4	0.1	41.4	0.00 / 0.00 / 0.00
79	0.4	63.5	1.2	19.5	0.00 / 2.94 / 8.82
88	5.0	48.6	17.7	39.2	0.00 / 0.00 / 0.00
92	1.3	46.1	22.8	34.0	0.00 / 0.00 / 0.00
100	0.5	50.0	0.8	3.3	2.94 / 5.88 / 5.88

Table 10. Detailed evaluation of the errors for solver ($D, 3, 7$) in the single-view setting. For every sequence of Fastec [44], we give the median and the minimum rotation and translation error, as well as the percentage of pose errors below 10° , 20° , 30° .

Seq	Median tensor error	Minimum tensor error
4	0.79	0.33
9	0.74	0.23
10	0.74	0.24
11	0.63	0.20
13	0.61	0.07
16	0.77	0.63
17	0.72	0.30
18	0.93	0.46
20	0.73	0.32
21	1.12	0.72
32	0.93	0.49
50	0.67	0.40
64	1.37	0.52
74	1.41	1.41
76	1.15	0.87
79	0.52	0.10
88	0.79	0.53
92	0.57	0.25
100	0.86	0.26

Table 11. Detailed evaluation of the errors for solver ($B, 3, 7$) in the multi-view setting. For every sequence of Fastec [44], we give the median and the minimum tensor error.

Seq	Median error	Minimum error
4	0.84	0.75
9	0.87	0.06
10	0.84	0.81
11	0.81	0.32
13	0.86	0.44
16	0.86	0.83
17	0.84	0.15
18	0.90	0.53
20	0.84	0.82
21	0.47	0.08
32	0.84	0.77
50	0.91	0.88
64	0.77	0.66
74	2.00	2.00
76	0.80	0.58
79	1.05	0.40
88	0.83	0.80
92	0.80	0.78
100	0.82	0.04

Table 12. Detailed evaluation of the errors for solver ($B, 3, 7$) in the single-view setting. For every sequence of Fastec [44], we give the median and the minimum tensor error.